
A KOLMOGOROV–ARNOLD NEURAL MODEL FOR CASCADING EXTREMES

Miguel de Carvalho
 School of Mathematics
 University of Edinburgh
 EH9 3FD, Edinburgh, UK
 Miguel.deCarvalho@ed.ac.uk

Clemente Ferrer
 Department of Mathematics
 Universidad Técnica Federico Santa Maria
 Valparaíso, Chile
 Clemente.Ferrer@usm.cl

Ronny Vallejos
 Department of Mathematics
 Universidad Técnica Federico Santa Maria
 Valparaíso, Chile
 Ronny.Vallejos@usm.cl

ABSTRACT

This paper addresses the growing concern of cascading extreme events, such as an extreme earthquake followed by a tsunami, by presenting a novel method for risk assessment focused on these domino effects. The proposed approach develops an extreme value theory framework within a Kolmogorov–Arnold network (KAN) to estimate the probability of one extreme event triggering another, conditionally on a feature vector. An extra layer is added to the KAN’s architecture to enforce the definition of the parameter of interest within the unit interval, and we refer to the resulting neural model as KANE (KAN with Natural Enforcement). The proposed method is backed by exhaustive numerical studies and further illustrated with real-world applications to seismology and climatology.

Keywords Bernoulli process · Chained extreme events · KAN · Kolmogorov superposition theorem · Neural network · Multivariate extremes · Regression models for extremes

1 Introduction

Record-breaking extreme events—such as catastrophic wildfires, unprecedented flooding, intense hurricanes, and unparalleled heatwaves—underscore the urgent need to strengthen our quantitative understanding of these occurrences. Extreme Value Theory (EVT) offers a solid mathematical framework, leveraging regular variation and asymptotic principles to estimate risks of such events by extrapolating beyond the limits of available data, into the tails of a distribution (Coles, 2001; Beirlant et al., 2004; de Haan and Ferreira, 2006; Resnick, 2007).

While it is widely recognized by practitioners that extreme events tend to occur in complex sequential forms (Cutter, 2018; Raymond et al., 2020), statistical modelling of this context from an EVT viewpoint is still underdeveloped. Multivariate EVT, though a natural starting point, falls short by: i) disregarding the triggering role of certain events; ii) overlooking the order and sequential nature of extreme event cascades; iii) lacking the ability to model feedback loops between events.

Inspired by the multivariate EVT framework, this paper introduces a novel concept—the POC (Probability of Cascade) surface—which assesses the probability of domino effects between extreme events conditionally on a covariate or feature vector $\mathbf{x} = (x_1, \dots, x_p)^\top$. As it will be shown below, the POC surface can be interpreted as the probability of a cascading extremal event, as it quantifies the probability that a trigger event (such as an earthquake exceeding magnitude u) results in a follow-up event (like a subsequent tsunami) as a function of a covariate. The proposed POC-based approach is fully general in the sense that the focus can be placed beyond the case where follow-up event is binary. In particular, we extend the framework to a multi-class setting, allowing for different types of follow-up extreme events,

and to an ordinal context, enabling follow-up extreme events to vary in ordinal severity. The case where the follow-up event is continuous includes as a special case the conditional coefficient of extremal dependence introduced by Lee et al. (2024).

To learn about the POC surface from the data, we develop a neural model grounded on Kolmogorov’s superposition theorem.¹

Theorem 1 (Kolmogorov’s superposition theorem). *Let $f : [0, 1]^d \rightarrow \mathbb{R}$ be a continuous function. Then, f can be expressed as follows*

$$f(\mathbf{x}) = \sum_{i=1}^{2d+1} \Phi_i^{(2)} \left(\sum_{j=1}^d \Phi_{i,j}^{(1)}(x_j) \right), \quad \mathbf{x} = (x_1, \dots, x_d)^\top, \quad (1)$$

for some continuous one-dimensional functions $\Phi_{i,j}^{(1)}$ and $\Phi_j^{(2)}$.

As it will be noted below, the beauty of this theorem is equally profound from both Mathematical and AI perspectives.

Mathematically speaking, it shows that any multivariate continuous function can be represented using only sums and univariate functions; the word superposition in this context refers to functions of functions, so that, for example,

$$f(x_1, x_2, x_3) = g(a(\alpha(x_1), \beta(x_2, x_3)), b(x_1, x_2)), \quad (2)$$

is a superposition of univariate and bivariate functions. Hence, in this sense, Theorem 1 shows that all multivariate continuous functions can be reduced to sums and superpositions of univariate functions.

From an AI perspective, the theorem reveals a two-layer neural network architecture recently popularized by Liu et al. (2024) following their extension to deeper settings. While multi-layer perceptrons are inspired by the universal approximation theorem (e.g., Berlyand and Jabin, 2023; Bishop and Bishop, 2023), Kolmogorov–Arnold Networks (KAN) are a novel and fast-evolving addition to the AI toolbox, and are rooted on Theorem 1. A particularly impressive aspect of KAN is that they are based on the principle any multivariate continuous function can be expressed exactly using only $2d + 1$ outer functions and d inner functions. In addition to the many developments following Liu et al., it should be noted that other neural approaches based on Theorem 1 had already appeared in the literature (Lin and Unbehauen, 1993; Sprecher and Draghici, 2002; Montanelli and Yang, 2020; Fakhoury et al., 2022).

Motivated by Theorem 1, we propose a neural model for the POC surface, constructing a network based on sums and superpositions of univariate functions. To ensure the resulting POC surface remains within the unit interval, an additional layer is incorporated into the architecture. This results in a three-layer design that enforces the unit interval constraint inherent to POC surfaces. The same principle can be applied to enforce any range constraint that the final output of a KAN may need to obey, and we refer to this neural model as KANE (Kolmogorov–Arnold Network with Natural Enforcement). We then extend the proposed network to a deep setting by a similar approach as in Liu et al. (2024). Finally, each univariate function in the Kolmogorov superposition representation is modeled using splines, and we provide theoretical guarantees on the model’s flexibility by drawing on approximation results for splines. As a byproduct, this paper contributes to the fast-evolving literature on interfaces between EVT and AI (e.g., Bhatia et al., 2021; Allouche et al., 2022; Karpov et al., 2022; NS et al., 2024, and references therein).

Finally, we note that our focus differs from that of Hawkes processes (Laub et al., 2021) in a number of important ways. The main difference is that our approach should be understood as an extension of the notion of tail dependence coefficient—aiming at quantifying conditional probabilities of extreme events—rather than an attempt to model self-excitation of processes.

The remainder of this paper is structured as follows. In Section 2, we introduce the proposed methods. Section 3 elaborates on extensions. Section 4 assesses the performance of the proposed methods through a series of numerical experiments conducted on simulated data. Empirical illustrations are provided in Section 5. Proofs and technical details are provided in the Appendix, whereas the online supplementary material includes additional computational experiments.

2 Neural Modeling of Cascading Extremes

2.1 The POC (Probability of Cascade) Surface

Let $I = \{I_u : u \in \mathbb{R}\}$ be a Bernoulli process (i.e., a random process with a Bernoulli marginal distributions), and let $Y \sim F_Y$ be a continuous random variable. We start by introducing the following functional, referred to as alpha, which

¹This result is also known as Kolmogorov–Arnold representation theorem. Among other things, it is well-known for refuting a conjecture implicit in Hilbert’s 13th problem presented in 1900 at the International Congress of Mathematicians.

plays a central role in our developments:

$$\alpha \equiv \alpha_I = \lim_{u \rightarrow y^*} P(I_u = 1 \mid Y > u). \quad (3)$$

Here and below, $y^* = \sup\{y : F_Y(y) < 1\}$ is the right endpoint of F_Y .

Loosely, the parameter $\alpha \in [0, 1]$ in (3) can be interpreted as the probability of a cascading event, where it quantifies the probability that a *trigger event* (such as an earthquake exceeding magnitude u) would result in a *follow-up event* (like a subsequent tsunami $I_u = 1$). The nature of the Bernoulli process I defining the follow-up event opens up a variety of modeling possibilities as illustrated below. Particularly, the Bernoulli process may depend on a continuous variable Z .

Example 1 (Tail dependence coefficient). If $I_u = I(Z > u)$, where Y and Z have common distribution, then

$$\alpha^{\text{TDC}} \equiv \alpha_I = \lim_{u \rightarrow y^*} P(Z > u \mid Y > u). \quad (4)$$

Thus, α in (3) includes the well-known tail dependence coefficient (Coles, 2001, Chapter 8) as a special case, specifically when the follow-up event involves Z being extreme, with Z being observable. ■

Example 2 (Extremal probabilistic index). If the follow-up event is that Z exceeds Y , then $I_u = I(Z > Y)$, and hence

$$\alpha^{\text{PI}} \equiv \alpha_I = \lim_{u \rightarrow y^*} P(Z > Y \mid Y > u), \quad (5)$$

which can be regarded as extremal version of the probabilistic index (Thas et al., 2012). Indeed, if X and Z are independent, then $\alpha^{\text{PI}} = P(Z > Y)$. Say, from a reliability analysis viewpoint, the extremal probabilistic index in (5) represents the probability of strength (Z) to be larger than stress (Y), given that stress is extreme. ■

Our setup keeps in mind that for some applications the variable Z in the above examples might be latent, but it assumes that the Bernoulli process I is observable. For instance, in the context of Example 1, we assume occurrence, or not, of a tsunami (I) is observable, even if its intensity level (Z) might be unavailable, whereas in the context of Example 2, we assume that the collapse, or not, of a system (I) is observable, even if its strength (Z) is not observable.

In practice it is desirable to assess how the α functional may be impacted by a covariate or feature. The POC (Probability of Cascade) surface, to be introduced below, naturally extends (3) to this covariate-adjusted framework as follows; without loss of generality, we assume the features are scaled to the unit interval.

Definition 1 (POC Surface). Let $\mathbf{x} = (x_1, \dots, x_d)^\top \in [0, 1]^d$. The probability of cascade surface is defined as

$$\text{POC} = \{(\mathbf{x}, \alpha_I(\mathbf{x})) : \mathbf{x} \in [0, 1]^d\}, \quad \alpha_I(\mathbf{x}) = \lim_{u \rightarrow y^*} P(I_{u, \mathbf{x}} = 1 \mid Y_{\mathbf{x}} > u), \quad (6)$$

where $I = \{I_{u, \mathbf{x}} : (u, \mathbf{x}) \in \mathbb{R} \times [0, 1]^d\}$ is a random field with Bernoulli marginal distributions and $\{Y_{\mathbf{x}} : \mathbf{x} \in [0, 1]^d\}$ is a random field.

In the case of a single covariate, we will refer to the POC surface as the POC curve. Although the POC surface is not invariant to continuous monotone transformations of the trigger event, it remains unchanged if the Bernoulli process threshold is adjusted accordingly.

Proposition 1. Let $h : \mathbb{R} \rightarrow \mathbb{R}$ be a strictly increasing function and let

$$\alpha_I^h(\mathbf{x}) = \lim_{u \rightarrow h(y^*)} P\{I_{h^{-1}(u), \mathbf{x}} = 1 \mid h(Y_{\mathbf{x}}) > u\}.$$

Then, $\alpha_I(\mathbf{x}) = \alpha_I^h(\mathbf{x})$, for any $\mathbf{x} \in [0, 1]^d$.

Proof. First, note that $\{h(Y_{\mathbf{x}}) > u\} = \{Y_{\mathbf{x}} > h^{-1}(u)\}$; also, by a change of variables $v = h^{-1}(u)$, it follows that if $u \rightarrow h(y^*)$, then $v \rightarrow y^*$. Thus,

$$\begin{aligned} \alpha_I^h(\mathbf{x}) &= \lim_{u \rightarrow h(y^*)} P\{I_{\mathbf{x}, h^{-1}(u)} = 1 \mid h(Y_{\mathbf{x}}) > u\} \\ &= \lim_{u \rightarrow h(y^*)} P\{I_{\mathbf{x}, h^{-1}(u)} = 1 \mid Y_{\mathbf{x}} > h^{-1}(u)\} \\ &= \lim_{v \rightarrow y^*} P\{I_{\mathbf{x}, v} = 1 \mid Y_{\mathbf{x}} > v\} \\ &= \alpha_I(\mathbf{x}). \end{aligned}$$

□

2.2 KANE: KAN with Natural Enforcement

A Kolmogorov–Arnold Approach for Learning from Data

Kolmogorov’s superposition theorem suggests a direct approach to modeling the POC surface using a standard KAN framework, by specifying

$$\alpha_I(\mathbf{x}) = \sum_{i=1}^{2d+1} \Phi_i^{(2)} \left(\sum_{j=1}^d \Phi_{i,j}^{(1)}(x_j) \right). \quad (7)$$

While theoretically appealing, the formulation in (7) does not ensure that in practice $\alpha_I(\mathbf{x})$ lies within its ‘natural’ interval, $[0, 1]$. This arises because the true $\alpha_I(\mathbf{x})$ is unknown in practice, requiring the inner and outer functions to be modeled and inferred from the data.

A straightforward solution is to include a final activation function in the architecture to ‘enforce’ this constraint. Let $g : \mathbb{R} \rightarrow [0, 1]$ be an activation function, and set

$$\alpha_I(\mathbf{x}) = g \left(\sum_{i=1}^{2d+1} \Phi_i^{(2)} \left(\sum_{j=1}^d \Phi_{i,j}^{(1)}(x_j) \right) \right). \quad (8)$$

Natural candidates to enforce the unit interval constraint include, for example, the sigmoid activation function,

$$g(x) = \frac{1}{1 + \exp(-x)}. \quad (9)$$

To distinguish the canonical KAN from our approach of enforcing the unit interval constraint, we refer to (8) as KANE (KAN with Natural Enforcement).² See Figure 1 for a schematic representation of the architecture of a three-layer KANE model. In function-matrix notation, KANE can be written as

$$\alpha_I(\mathbf{x}) = g \left((\Phi^{(2)} \circ \Phi^{(1)})(\mathbf{x}) \right),$$

where

$$\Phi^{(2)} = \begin{pmatrix} \Phi_1^{(2)} \\ \vdots \\ \Phi_{2d+1}^{(2)} \end{pmatrix}^\top, \quad \Phi^{(1)} = \begin{pmatrix} \Phi_{1,1}^{(1)} & \cdots & \Phi_{1,d}^{(1)} \\ \vdots & \ddots & \vdots \\ \Phi_{2d+1,1}^{(1)} & \cdots & \Phi_{2d+1,d}^{(1)} \end{pmatrix}.$$

We use the following terminology for the layers of KANE: $\Phi^{(1)}$ refers to the *input layer*, $\Phi^{(2)}$ to the *pre-output layer*, whereas g represents the *g-layer* which is responsible for transforming the pre-output into the unit interval.

Modeling via Splines

For convenience, in what follows we denote the outer function as $\Phi_i^{(2)}$ or $\Phi_{1,i}^{(2)}$ depending on what is typographically convenient, a choice whose justification will become apparent once the spline formulation and the deep version of the model are introduced.

Consider $m + 1$ equally-spaced knots, $t_0 < \cdots < t_m$. We model the inner and outer functions as a linear combination of B-spline basis functions, that is, for $l = 1, 2$,

$$\Phi_{i,j}^{(l)}(x) = \sum_{k=1}^K \beta_{i,j,k}^{(l)} B_k^p(x),$$

where $B_k^p(x)$ is the B-spline basis function of degree p evaluated at x and $K = p + m$. For $l = 1$ it follows that $i \in \{1, \dots, 2d+1\}$ and $j \in \{1, \dots, d\}$, whereas for $l = 2$ it holds that $i \in \{1\}$ and $j \in \{1, \dots, 2d+1\}$. To streamline the notation, we assume the same number of basis functions K per univariate function and the same set of knots, a choice made for convenience that can be adjusted at the cost of more complex notation. The parameter of interest is given by the $(2d+1) \times (d+1) \times K$ partitioned tensor

$$\beta = (\beta_k^{(1)} \mid \beta_k^{(2)}),$$

²Naturally, for other contexts other range constraints can be similarly enforced using alternative activation functions (e.g., $g(x) > 0$ if the target of interest is positive), but a mapping to the unit interval is all we need for modeling the POC surface.

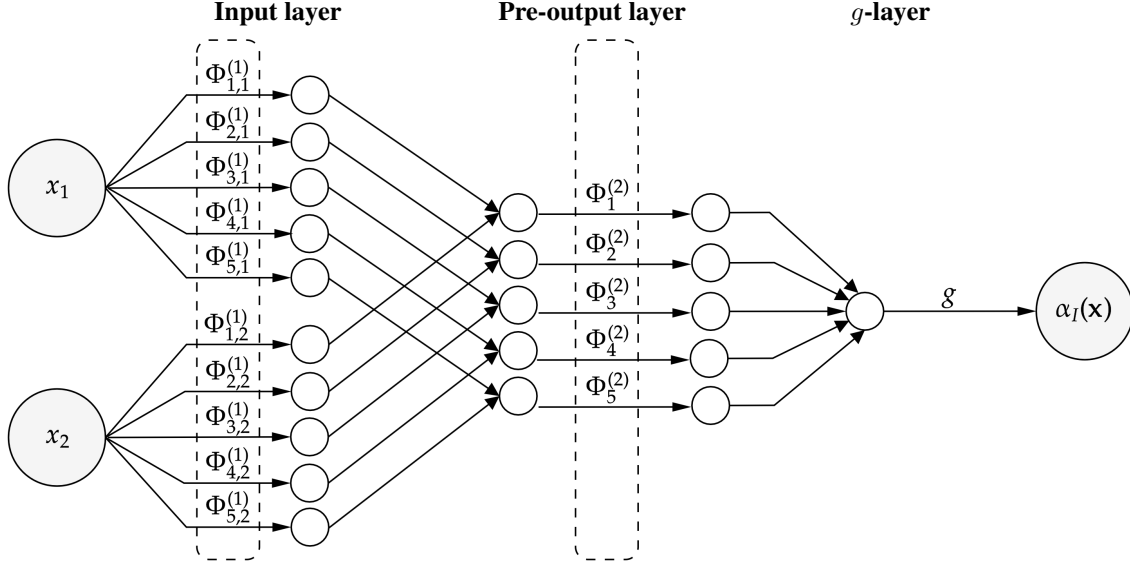


Figure 1: Architecture of three-layer KANE model for the POC surface (binary follow-up event) illustrated on two-feature setting.

where for $k = 1, \dots, K$,

$$\beta_k^{(1)} = \begin{pmatrix} \beta_{1,1,k}^{(1)} & \cdots & \beta_{1,d,k}^{(1)} \\ \vdots & \ddots & \vdots \\ \beta_{2d+1,1,k}^{(1)} & \cdots & \beta_{2d+1,d,k}^{(1)} \end{pmatrix}, \quad \beta_k^{(2)} = \begin{pmatrix} \beta_{1,1,k}^{(2)} \\ \vdots \\ \beta_{2d+1,1,k}^{(2)} \end{pmatrix}.$$

To learn about the POC surface from data—that is, to infer about the tensor β —we base our inferences on

$$D_n = \{(\delta_i, \mathbf{x}_i) : y_i > u\}_{i=1}^n,$$

for a sufficiently large threshold u . Here, $\delta_i, y_i, \mathbf{x}_i$ are respectively realizations from $I_{u,\mathbf{x}}$ and $Y_{\mathbf{x}}$, given $\mathbf{X} = \mathbf{x}$. The tensor β is estimated by minimizing the binary cross-entropy loss,

$$L(\beta) = -\frac{1}{n} \sum_{i=1}^n \{\delta_i \log(\alpha_I(\mathbf{x}_i)) + (1 - \delta_i) \log(1 - \alpha_I(\mathbf{x}_i))\}.$$

The minimizer of L , denoted as $\hat{\beta}$, is used to obtain the KANE estimate of the POC surface, $\hat{\alpha}_I(\mathbf{x}_i)$, as a plug-in estimator in (8). While the asymptotic normality of the resulting estimator remains an open question for future research, the supplementary materials provide numerical evidence that confidence intervals obtained via a resampling cases bootstrap seem to perform reasonably well, with coverage close to the nominal level.

Deep KANE

A deep KANE model for the POC surface can be readily obtained following the same line of attack as in Liu et al. (2024). That is, the deep KANE formulation is based on the following L -layer specification,

$$\alpha_I(\mathbf{x}) = g\left((\Phi^{(L-1)} \circ \cdots \circ \Phi^{(1)})(\mathbf{x})\right),$$

where for $l \in \{1, \dots, L-1\}$,

$$\Phi^{(l)} = \begin{pmatrix} \Phi_{1,1}^{(l)} & \cdots & \Phi_{1,n_l}^{(l)} \\ \vdots & \ddots & \vdots \\ \Phi_{n_{l+1},1}^{(l)} & \cdots & \Phi_{n_{l+1},n_l}^{(l)} \end{pmatrix}.$$

Here, n_l is the number of nodes in the l th layer, for $l = 1, \dots, L$. The three-layer KANE presented above is a particular case with $n_1 = d$, $n_2 = 2d + 1$, and $n_3 = 1$. For modeling in the deep framework we again use the specification in (2.2). The parameter of interest in this case is given by the following collection of matrices

$$\beta_k^{(l)} = \begin{pmatrix} \beta_{n_l,1,k}^{(l)} & \cdots & \beta_{n_l,d,k}^{(l)} \\ \vdots & \ddots & \vdots \\ \beta_{n_{l+1},1,k}^{(l)} & \cdots & \beta_{n_{l+1},d,k}^{(l)} \end{pmatrix},$$

where $k = 1, \dots, K$ and $l = 1, \dots, L$.

2.3 Model Checking and Diagnostics

For evaluating the quality of the fit from the KANE model, we resort to randomized quantile residuals introduced by Dunn and Smyth (1996). Before we present the version of these residuals for our model, we recall that their basic principle is as follows: For any nonparametric or parametric model, based on a continuous distribution function, $F(x) = P(X \leq x)$, it follows that $R \equiv \Phi^{-1}(F(X)) \sim N(0, 1)$, when $X \sim F$, where Φ^{-1} is the standard normal quantile function. Hence, provided that F is a sensible model for the data X , then the residuals R are a normal distributed. As noted by Dunn and Smyth, the same principle can be easily extended to a discrete model F via jittering. Since for each fixed u , our POC surface formulation can be understood as binary response regression model based on D_n , it follows that its Dunn–Smyth residuals are defined as

$$R_i = \begin{cases} \Phi^{-1}(W_i), & \delta_i = 1, \\ \Phi^{-1}(V_i), & \delta_i = 0, \end{cases} \quad \text{with} \quad V_i \sim \text{Unif}(0, 1 - \hat{\alpha}(\mathbf{x}_i)), \quad W_i \sim \text{Unif}(1 - \hat{\alpha}(\mathbf{x}_i), 1).$$

Loosely, the R_i are a jittered version of the ‘binary response’ (i.e., follow-up event δ_i), with the level of jittering being controlled by the ‘probability of success’ (i.e., probability of cascade $\hat{\alpha}(\mathbf{x}_i)$). We recommend reporting at least 10 trajectories of the randomized quantile residuals, noting that Dunn and Smyth (1996) suggested that “four realizations of the quantile residual” would already be sufficient. These realizations will be presented in a QQ-boxplot along with the confidence bands stemming from the normal reference model (that keeps in mind that the R_i are normal distributed provided that the fit is sensible); the QQ-boxplot was recently introduced by Rodu and Kafadar (2021), and consists of a graphical tool that merges into a single chart a boxplot and a QQ-plot.

3 Consequences and Extensions

3.1 Multi-Trigger Systems

In practice, multiple competing incidents can result in the follow-up event. To address this, we define a multi-trigger system where we consider $\mathcal{Y}_1, \dots, \mathcal{Y}_K$ as a sequence of identically distributed random fields with

$$\mathcal{Y}_k = \{Y_{k,\mathbf{x}} : \mathbf{x} \in [0, 1]^d\}, \quad k = 1, \dots, K.$$

Our framework extends to K trigger events by considering

$$\alpha(\mathbf{x}) = \lim_{u \rightarrow y^*} P(I_{u,\mathbf{x}} = 1 \mid Y_{1,\mathbf{x}} > u \vee \dots \vee Y_{K,\mathbf{x}} > u). \quad (10)$$

This formula simplifies to the single-trigger case in (6) by defining $Y_{\mathbf{x}} = \min\{Y_{1,\mathbf{x}}, \dots, Y_{K,\mathbf{x}}\}$, and hence the theory and methods from Section 2 readily apply to this context as well. The identically distributed assumption for $\mathcal{Y}_1, \dots, \mathcal{Y}_K$ is for convenience, as in practice random processes can be normalized to a common scale (say, unit Fréchet margins) using the probability integral transform.

3.2 Categorical, Ordinal, and Continuous Follow-up Events

In real-world applications, follow-up extreme events can take various forms, including multicategorical, ordinal, and continuous outcomes. As examples of categorical and ordinal events: For instance, $j = 1$ may represent ‘no tornado’, $j = 2$ a ‘supercell tornado’, and $j = 3$ a ‘non-supercell tornado’. Similarly, $j = 1$ to $j = 5$ may represent Category 1 to Category 5 hurricanes.

In the multicategorical context, we model the follow-up event as a multinoulli process, that is,

$$\mathbf{I} = \{\mathbf{I}_{u,\mathbf{x}} : (u, \mathbf{x}) \in \mathbb{R} \times [0, 1]^d\},$$

is a random field with multinoulli marginal distribution. Here, $\mathbf{I}_{u,\mathbf{x}} = (I_{u,\mathbf{x}}^{(1)}, \dots, I_{u,\mathbf{x}}^{(J)})^\top \in \{0, 1\}^J$ and J is the number of categories; see Murphy (2012, Section 2.3.2) for basics on the multinoulli distribution. The proposed cascading probability extends to this context as follows.

Definition 2 (Multicategorical POC Surfaces). *Let $\mathbf{x} = (x_1, \dots, x_d)^\top \in [0, 1]^d$ and $J \in \mathbb{N}$. The j th-category probability of cascade surface is defined as*

$$\text{POC}_j = \{(\mathbf{x}, \alpha_{\mathbf{I}}^{(j)}(\mathbf{x})) : \mathbf{x} \in [0, 1]^d\}, \quad \alpha_{\mathbf{I}}^{(j)}(\mathbf{x}) = \lim_{u \rightarrow y^*} P(\mathbf{I}_{u,\mathbf{x}}^{(j)} = 1 \mid Y_{\mathbf{x}} > u), \quad (11)$$

for $j \in \{1, \dots, J\}$, where $\mathbf{I} = \{\mathbf{I}_{u,\mathbf{x}} : (u, \mathbf{x}) \in \mathbb{R} \times [0, 1]^d\}$ is a multinoulli process and $\{Y_{\mathbf{x}} : \mathbf{x} \in [0, 1]^d\}$ is a random field.

In terms of fitting the model, two adjustment are needed for the architecture discussed in Section 2. Firstly, we need an activation function for the g -layer that maps the Euclidean space to the unit simplex; that is, $\mathbf{g} = (g^{(1)}, \dots, g^{(J)})$, where $g^{(j)} : \mathbb{R}^d \rightarrow [0, 1]$, such that $\sum_{j=1}^J g^{(j)}(\mathbf{x}) = 1$. A natural candidate for this task is the softmax activation function, in which case the g -layer becomes,

$$g^{(j)}(\mathbf{x}) = \frac{\exp(x_j)}{\sum_{j=1}^J \exp(x_j)}. \quad (12)$$

Secondly, the loss function must account for the different categories, for which the cross-entropy loss is employed

$$L(\beta) = -\frac{1}{n} \sum_{i=1}^n \sum_{j=1}^J \{\delta_{i,j} \log(\alpha_{\mathbf{I}}^{(j)}(\mathbf{x}_i)) + (1 - \delta_{i,j}) \log(1 - \alpha_{\mathbf{I}}^{(j)}(\mathbf{x}_i))\},$$

where $(\delta_{i,1}, \dots, \delta_{i,J})^\top$ is a realization of $\mathbf{I}_{u,\mathbf{x}_i}$.

Relatedly, the follow-up extremal event may have a natural ordered category. The formal definition of the POC surface for this case is tantamount to the one provided in (11). When fitting the model, ordinal events must be handled carefully, avoiding the mistake of treating categories as nominal quantities. For example, a naïve approach would be to apply the aforementioned multicategorical framework with a softmax activation function, but this would ignore the ordinal structure in the data. Instead, a simple alternative to address this issue is by devising a version of the well-known approach by Frank and Hall (2001) to our setting; see also Alcacer et al. (2024).

The Frank–Hall approach begins by transforming a J -class ordinal problem into $J - 1$ binary classification problems. Specifically, an ordinal attribute A with ordered values C_1, \dots, C_J is converted into $J - 1$ binary attributes of the form $A > C_j$, for $j = 1, \dots, J - 1$; for example, on the above-mentioned $J = 5$ hurricane problem, this would imply converting the original ordinal problem into four binary attributes based on

$$A > \text{Category } 1, \quad A > \text{Category } 2, \quad A > \text{Category } 3, \quad A > \text{Category } 4.$$

Hence, the probabilities for each category for the Frank–Hall approach are given by $P(C_1) = 1 - p_1$,

$$P(C_j) = p_{j-1} - p_j, \quad j = 2, \dots, J - 1,$$

and $P(C_J) = p_{J-1}$, where $p_j = P(A > C_j)$, for all j .

Based on this, the ordinal multicategorical POC surface can be derived. Let $\mathbf{A}_{u,\mathbf{x}}$ be an ordinal attribute, and define $\pi_j(\mathbf{x}) = \lim_{u \rightarrow y^*} P(\mathbf{A}_{u,\mathbf{x}} > C_1 \mid Y_{\mathbf{x}} > u)$. The Frank–Hall POC surface is then given by $\alpha_{\mathbf{I}}^{(1)}(\mathbf{x}) = 1 - \pi_j(\mathbf{x})$,

$$\alpha_{\mathbf{I}}^{(j)}(\mathbf{x}) = \pi_{j-1}(\mathbf{x}) - \pi_j(\mathbf{x}), \quad j = 2, \dots, J - 1,$$

and $\alpha_{\mathbf{I}}^{(J)}(\mathbf{x}) = \pi_{J-1}(\mathbf{x})$.

Finally, for a continuous-type follow-up event, if a continuous variable $Z_{\mathbf{x}}$ is observable—similar to Example 1—we can set $I_{u,\mathbf{x}} = I(Z_{\mathbf{x}} > u)$ in which case we obtain the conditional coefficient of extremal dependence by Lee et al. (2024).

4 Numerical Experiments on Artificial Data

4.1 Artificial Data Generating Processes and Preliminary Experiments

This section presents the simulation scenarios used to evaluate the proposed methods, along with a series of single-sample experiments. We assess performance in three settings by simulating $n = 10\,000$ observations per scenario, with

artificial data generated from the Bernoulli process, follow-up events, and features as described below. In each case, we threshold the response at its 95% quantile (u), hence retaining only those values where $Y_x > u$.

Scenarios A1 and A2: For these scenarios, the follow-up events are respectively simulated from Bernoulli processes with

$$I_{u,x} \mid Y_x > u \sim \text{Bern}\{m_{Ak}(x; u)\}, \quad k = 1, 2,$$

for $x \in [0, 1]$. For Scenario A1, $m_{A1}(x; u) = \Phi(x, \exp(-u), 1)$ is the distribution function of the normal distribution with mean $\exp(-u)$ and variance 1, whereas for Scenario A2, $m_{A2}(x; u) = 0.2 \sin\{3\pi(x-1)^2\} + 0.4 + 1/u^2$.

In both cases, we simulate a single feature X from the standard uniform distribution, and the trigger event $Y_x \mid X = x$ is generated from a unit Fréchet distribution. The true POC curves corresponding to $m_{A1}(x; u)$ and $m_{A2}(x; u)$ are respectively given by

$$\begin{cases} \alpha_I^{A1}(x) = \lim_{u \rightarrow \infty} m_{A1}(x; u) = \Phi(x, 0, 1), \\ \alpha_I^{A2}(x) = \lim_{u \rightarrow \infty} m_{A2}(x; u) = 0.2 \sin\{3\pi(x-1)^2\} + 0.4. \end{cases}$$

Scenarios B1 and B2: For these scenarios, the follow-up events are respectively simulated from a Bernoulli processes with

$$I_{u,\mathbf{x}} \mid Y_{\mathbf{x}} > u \sim \text{Bern}\{m_{Bk}(\mathbf{x}; u)\}, \quad k = 1, 2,$$

for $\mathbf{x} = (x_1, x_2) \in [0, 1]^2$. For Scenario B1, $m_{B1}(\mathbf{x}; u) = \Phi(\mathbf{x}; \exp(-u)\mathbf{1}_2, \mathbf{I}_2)$ is the bivariate distribution function of the bivariate normal distribution, whereas for Scenario B2, $m_{B2}(\mathbf{x}; u) = 0.4 \exp(-x_1) \cos\{2\pi x_2\} + 0.5 + 1/u^2$. In both cases, we simulate two independent features, X_1 and X_2 , which are drawn from the standard uniform distribution; the trigger event $Y_{\mathbf{x}} \mid (X_1, X_2) = (x_1, x_2)$ is again simulated from a unit Fréchet distribution. The true POC surfaces corresponding to $m_{B1}(\mathbf{x}; u)$ and $m_{B2}(\mathbf{x}; u)$ are respectively given by

$$\begin{cases} \alpha_I^{B1}(\mathbf{x}) = \lim_{u \rightarrow \infty} m_{B1}(\mathbf{x}; u) = \Phi(\mathbf{x}, 0, \mathbf{I}_2), \\ \alpha_I^{B2}(\mathbf{x}) = \lim_{u \rightarrow \infty} m_{B2}(\mathbf{x}; u) = 0.4 \exp(-x_1) \cos\{2\pi x_2\} + 0.5. \end{cases}$$

Scenario C: The final scenario examines a multi-category framework, as described in Section 3.2. The follow-up events are simulated from a multinoulli process with

$$\mathbf{I}_{u,\mathbf{x}} \mid Y_{\mathbf{x}} > u \sim \text{Multi}_3 \left(\frac{m_{C1}(\mathbf{x}; u)}{M_u}, \frac{m_{C2}(\mathbf{x}; u)}{M_u}, \frac{m_{C3}(\mathbf{x}; u)}{M_u} \right),$$

for $\mathbf{x} = (x_1, x_2)^\top \in [0, 1]^2$. Here, $M_u = m_{C1}(\mathbf{x}; u) + m_{C2}(\mathbf{x}; u) + m_{C3}(\mathbf{x}; u)$, where $m_{C1}(\mathbf{x}; u) = \Phi(\mathbf{x}; \exp(-u)\mathbf{1}_2, \mathbf{I}_2)$, $m_{C2}(\mathbf{x}; u) = 0.4 \exp(-x_1) \cos(2\pi x_2) + 0.5 + 1/u^2$, and $m_{C3}(\mathbf{x}; u) = 0.8x_2 \sin^2(\pi x_1) + 1/u^2$. The trigger event and features follow the same settings as in Scenarios B1 and B2 (i.e., the trigger is unit Fréchet-distributed and features are independently drawn from the standard uniform distribution). The true j th-category POC surfaces in this case are

$$\begin{cases} \alpha_I^{(1)}(\mathbf{x}) = \lim_{u \rightarrow \infty} \frac{m_{C1}(\mathbf{x}; u)}{M_u} = \frac{\Phi(\mathbf{x}; \mathbf{0}, \mathbf{I}_2)}{M}, \\ \alpha_I^{(2)}(\mathbf{x}) = \lim_{u \rightarrow \infty} \frac{m_{C2}(\mathbf{x}; u)}{M_u} = \frac{0.4 \exp(-x_1) \cos\{2\pi x_2\} + 0.5}{M}, \\ \alpha_I^{(3)}(\mathbf{x}) = \lim_{u \rightarrow \infty} \frac{m_{C3}(\mathbf{x}; u)}{M_u} = \frac{0.8x_2 \sin^2(\pi x_1)}{M}, \end{cases}$$

where

$$M = \Phi(\mathbf{x}; \mathbf{0}, \mathbf{I}_2) + 0.4 \exp(-x_1) \cos\{2\pi x_2\} + 0.8x_2 \sin^2(\pi x_1) + 0.5.$$

The results from a single-sample experiment are shown in Figure 2. As can be seen from the latter figures, the proposed methods satisfactorily recover the true POC in all scenarios; these findings should be considered provisional, as they come from a single-sample experiment, with the Monte Carlo performance to be evaluated next in Section 4.2.

Some final comments on computing and implementations are in order. The neural model was fitted using the LBFGS optimizer (Pytlak, 2008, Chapter 5). For binary classification scenarios, the sigmoid activation function (9) was specified for the g layer to ensure that the output values remain within the unit interval, representing valid probabilities. In cases of multi-category classification, the softmax activation function in (12) was used. The optimization process was carried out for 100 steps for each scenario, with $m = 2$ and $p = 3$, as cubic splines are continuous and have continuous first and second derivatives at each knot.

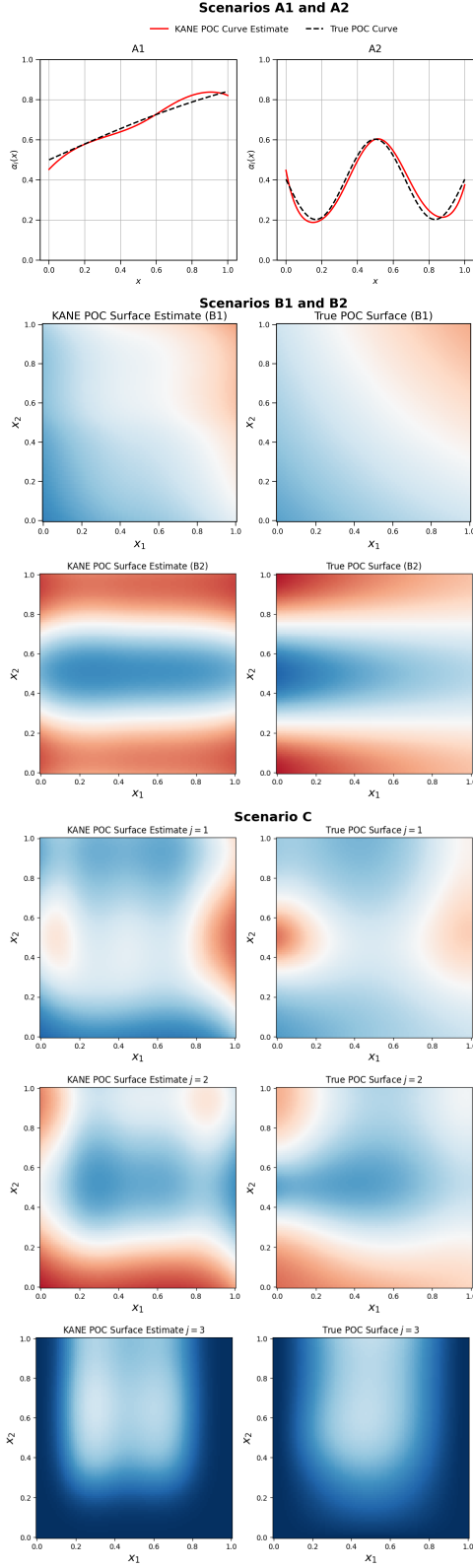


Figure 2: Single-sample experiments for Scenarios A, B, and C.

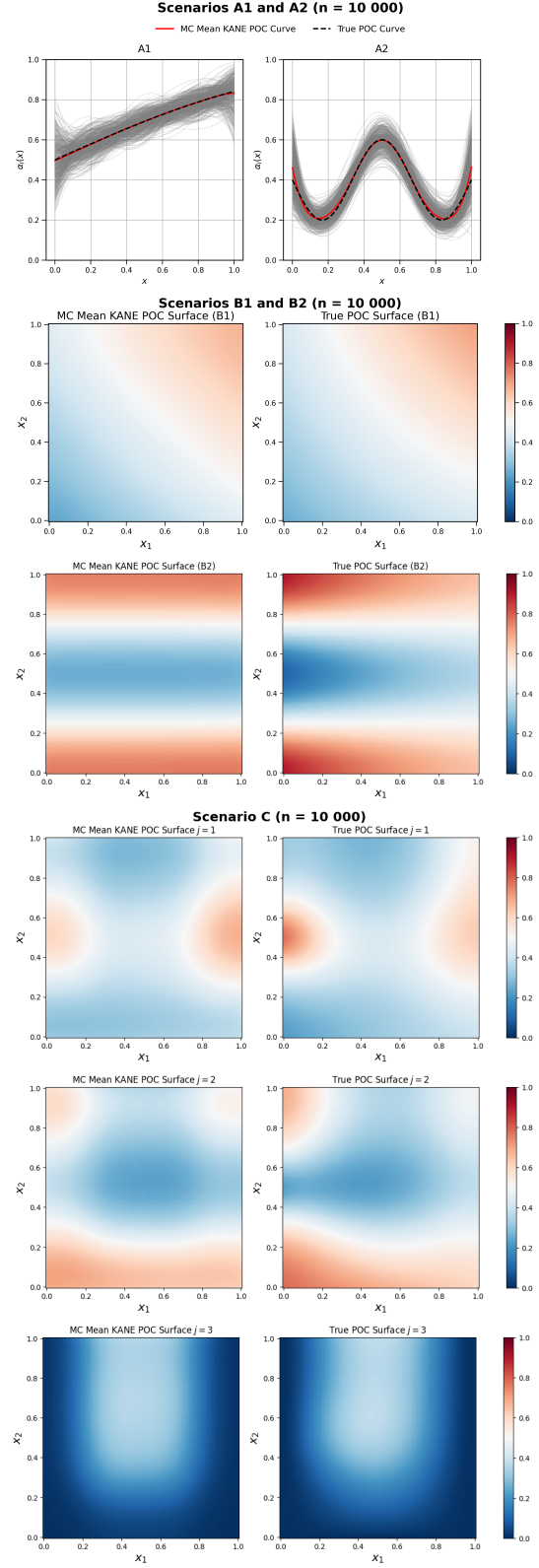


Figure 3: Monte Carlo means for Scenarios A, B, and C.

4.2 Monte Carlo Evidence

This section reports the main findings of a Monte Carlo simulation study, where we repeat $M = 500$ times the single-sample experiment from the previous section. We consider three sample sizes $n = 5000, 10\,000$, and $15\,000$. Figure 3 shows the Monte Carlo means of the simulation study, indicating strong performance across different scenarios, as anticipated by Figure 2.

Table 1: MISE values across scenarios and sample sizes.

Scenario	Sample Size		
	5 000	10 000	15 000
A1	9.112×10^{-6}	3.706×10^{-6}	7.759×10^{-7}
A2	1.501×10^{-4}	1.541×10^{-4}	1.478×10^{-4}
B1	1.021×10^{-4}	8.014×10^{-5}	7.722×10^{-5}
B2	2.669×10^{-3}	2.626×10^{-3}	2.625×10^{-3}
C ($j = 1$)	9.465×10^{-4}	9.055×10^{-4}	8.958×10^{-4}
C ($j = 2$)	1.166×10^{-3}	1.130×10^{-3}	1.106×10^{-3}
C ($j = 3$)	1.725×10^{-4}	1.185×10^{-4}	9.428×10^{-5}

Finally, in Table 1 we report the Monte Carlo MISE (Mean Integrated Squared Error), where

$$\text{MISE} = \int_{[0,1]^d} \{\hat{\alpha}_I(\mathbf{x}) - \alpha_I(\mathbf{x})\}^2 d\mathbf{x}.$$

Here, $\hat{\alpha}_I(\mathbf{x})$ is the KANE estimate of POC and $[0, 1]^d$ is the space of the features (i.e., $d = 1$ for Scenarios A1–A2, and $d = 2$ for Scenarios B1–B2 and C). As can be seen from Table 1, the proposed approach has appealing frequentist properties from a numerical viewpoint, in the sense that as the sample size increases, MISE decreases.

In the supplementary materials, we document a battery of additional Monte Carlo experiments, including analyses of dependent features, an evaluation of the deep model, and a comparison of the Frank–Hall ordinal model with the softmax approach. Among other findings, these additional results further validate the approach’s performance, show that performance is better in data-rich regions of the covariate space, and that the canonical three-layer model may perform as well as, if not better than, its deep counterpart.

5 Empirical Examples

5.1 Earthquake–Tsunami Data

Coastal regions are highly vulnerable to tsunamis, with their impacts often exacerbated by significant earthquakes that act as primary triggers. This section applies the proposed method to quantify the POC for tsunami occurrence ($I_{u,\mathbf{x}}$) triggered by extreme earthquakes ($Y_{\mathbf{x}} > u$).

Data were gathered from the NCEI/WDS Global Significant Earthquake Database, provided by the NOAA National Centers for Environmental Information, and consist of a point process data on earthquake locations (latitude and longitude) from 2150 B.C., including whether a tsunami followed or not. Figure 4 shows the spatial distribution of significant earthquakes and associated tsunamis.

The trigger events are thresholded at $u = F_{Y_{\mathbf{x}}}^{-1}(0.95)$, resulting in 167 observations of earthquakes with magnitudes greater than 7.9 on the Richter scale, along with the corresponding indicators of tsunami occurrence. The fitted POC surfaces were modeled according to Section 2.2, with a three-layer KANE framework following the setup from Section 4, and considering the features $\mathbf{x} = (\text{latitude}, \text{longitude}, \text{depth})^\top$.

As can be seen from Fig. 5, the fitted surface tends to be particularly pronounced, for example in the coast of Chile, California, and the Pacific ring in comparison with the Caribbean; the same figure also illustrates that POC tends to be low at greater depths (e.g., 85th percentile), hence suggesting that earthquakes which are deeper would less likely lead to a cascading tsunami event. All in all, the usual extrapolation disclaimer applies. Interpretations should account

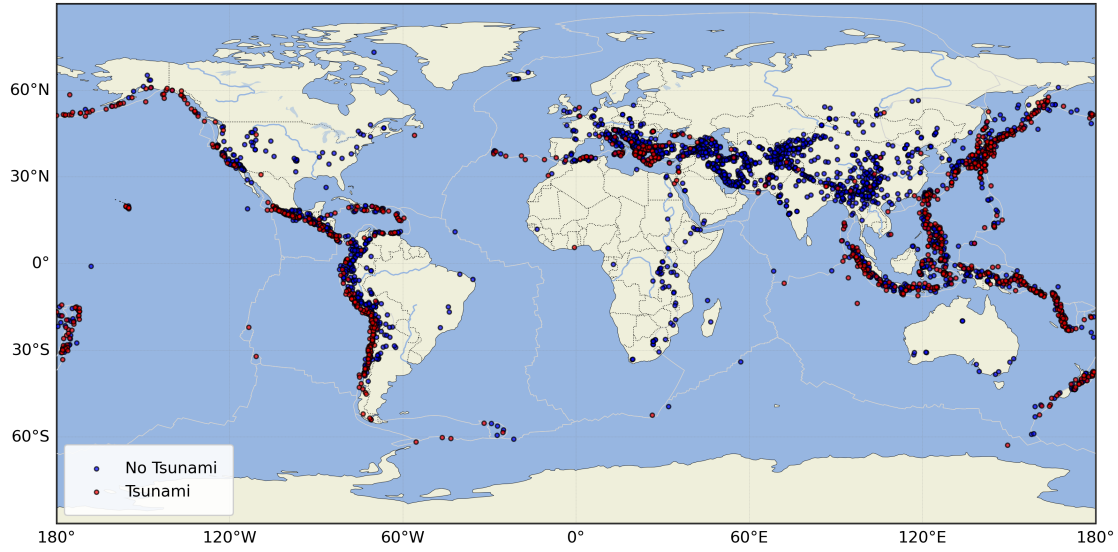


Figure 4: Point pattern of earthquakes (red) and associated tsunami occurrences (blue).

for the fact that the quality of the fits is more reliable in regions with greater data availability, while their accuracy should be questioned in regions with limited data. Finally, the QQ-boxplot of the randomized residuals, shown in Fig. 7, indicates an overall good fit; further trajectories in the supplementary materials indicate a similar finding.

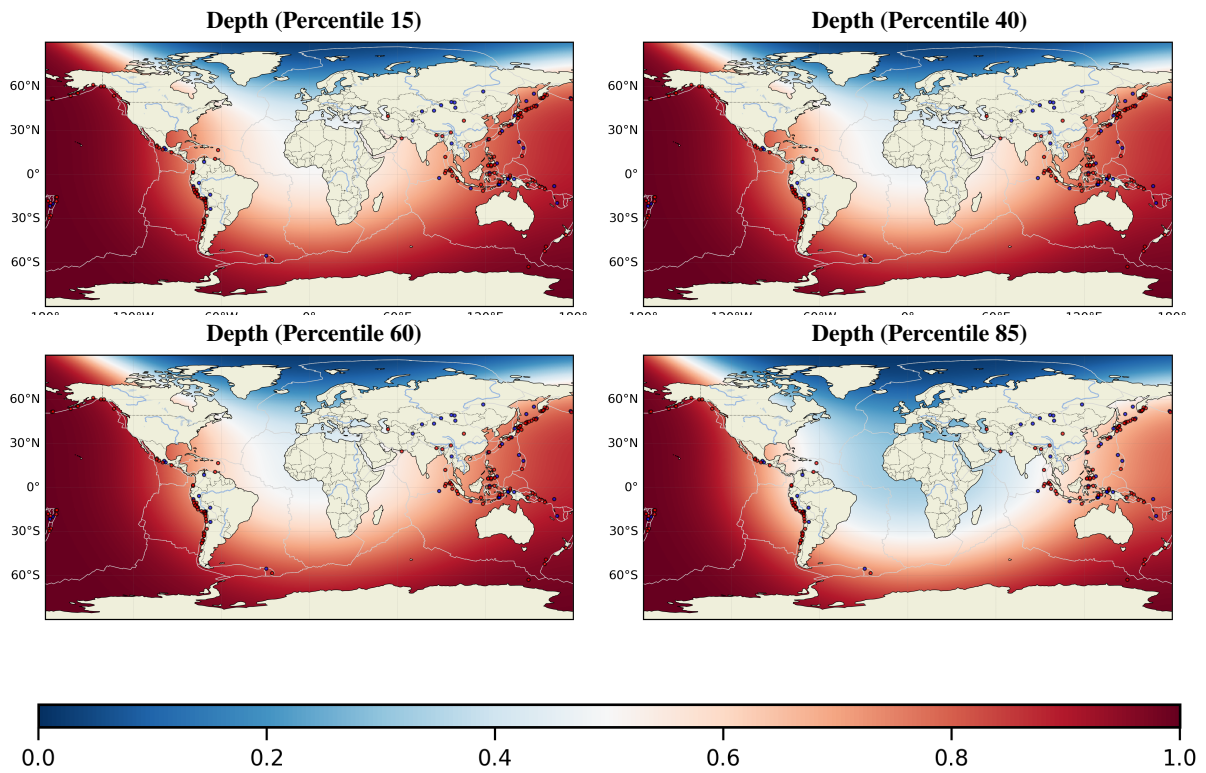


Figure 5: KANE POC surface estimate for Earthquake–Tsunami data, considering percentile 15, 40, 60, and 85 of depth.

5.2 Tropical Cyclone–Sea Surface Temperature Data

Rising sea surface temperature (SST) anomalies significantly impact coastal and oceanic regions, particularly by influencing tropical cyclone intensity—categorized as Tropical Depression, Tropical Storm, and Hurricane in the North Atlantic and Northeast Pacific. Our second illustration will shed light on the ordered multicategory POC surface for tropical cyclone types ($\mathbf{I}_{u,\mathbf{x}}$), conditional on extreme SST events ($Y_{\mathbf{x}} > u$).

Data were obtained from two complementary sources covering 1981–2016: The ESA Climate Change Initiative, which provides global daily-mean SST observations on a latitude-longitude grid, and the NOAA Atlantic Hurricane dataset, which contains six-hourly storm tracks. SST values exceeding $u = F_{Y_{\mathbf{x}}}^{-1}(0.95) = 302.74$ K define extreme trigger events, yielding 456 observations.

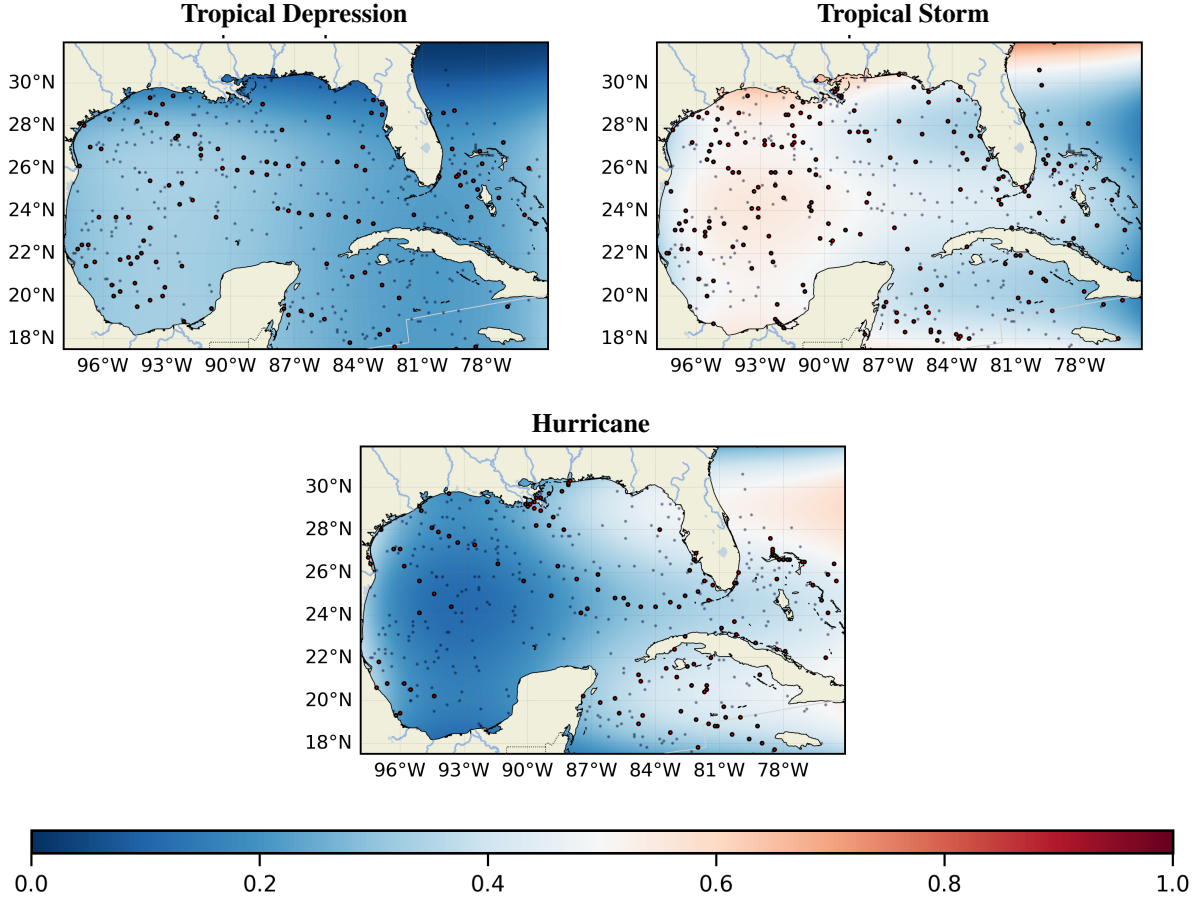


Figure 6: KANE POC surface estimate for Tropical Cyclone–SST data.

Keeping in mind the ordinal nature of the data, the fitted POC surfaces were modeled according to the Frank–Hall variant of our model (Section 3), with a three-layer KANE framework, and considering the features $\mathbf{x} = (\text{latitude}, \text{longitude})^T$. Among other insights, the fitted surfaces suggest that high sea surface temperatures tend to be associated with more extreme tropical storms in parts of Gulf of Mexico. Aside from this, the analysis also reveals that the probability of cascade remains relatively small for tropical depression and hurricanes. Finally, the QQ-boxplot of the randomized residuals is shown in Fig. 7 and suggests an overall good fit of the model; further trajectories, presented in the supplementary materials, provide comparable evidence.

6 Implications and Future Directions

This paper develops a novel statistical framework to address the growing concern of cascading extreme events—such as earthquakes triggering tsunamis or heatwaves sparking wildfires, which in turn lead to further losses. By integrating

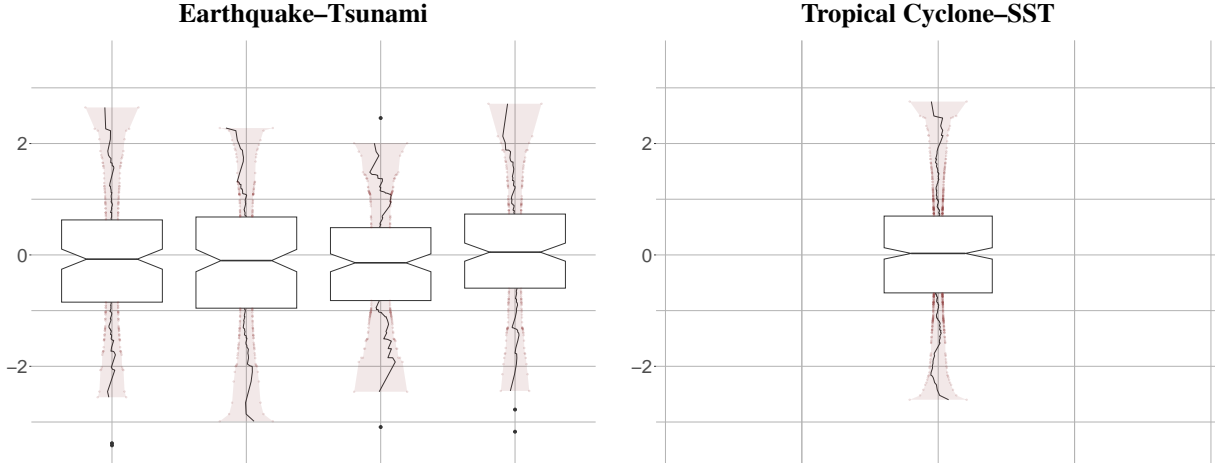


Figure 7: QQ-boxplots of Dunn–Smyth residuals for empirical illustrations.

EVT and AI, the proposed methods aim to enable extrapolation beyond observed data to capture and model complex chains of extreme events. Although straightforward, the additional ‘Natural Enforcement’ of KAN discussed in this work may be valuable for other applications. For instance, it could be relevant when modeling covariate-adjusted versions of other extreme value parameters, such as $\bar{\chi}$ (Coles, 2001, Chapter 8), which is constrained to the range $(-1, 1]$. This constraint could similarly be enforced naturally within our g -layer.

While KAN models have been claimed to be explainable (Liu et al., 2024), one might consider the possibility of fitting POC surfaces using a more conventional explainable statistical model. If explainability is a priority, the POC surfaces introduced above can be formulated as an additive generalized linear model along the same lines as in Lee et al. (2024).

We close the paper with some final comments on future research. In practice, either the follow-up or the trigger event may themselves be functional in the sense of FDA (Functional Data Analysis) (Horváth and Kokoszka, 2012; Kokoszka, 2017). For example, we may observe $I_{u,x} = 1$ for x over a *continuum* rather than over a point $x \in [0, 1]^d$. As a concrete instance of this, in the earthquake data application, a follow-up event could represent the full region $S \subset [0, 1]^2$ affected by the tsunami, in which case $I_{u,x} = 1$ for all $x \in S$. While our theory also accommodates this framework, further investigation is needed to incorporate such functional events into the inferences in a fully FDA-aligned fashion. Secondly, while there are fundamental differences between our approach and Hawkes processes, there may be interest in combining our framework with the cross-excitation of multiple point processes introduced by Hawkes (1971).

Finally, while the proposed approach targets two-chain setups involving a trigger and follow-up extreme event, it may set the stage for developments that accommodate extremal chains of random length (k), and also factoring in the role of the chain’s pathways. TDMs (Tail Dependence Matrices) (Embrechts et al., 2016) may be used to govern the pathway of the extremal cascade; in this setting the order of chained events could be dictated by a random permutation of $\{1, \dots, k\}$, based on transition probabilities for the TDMs between extremal events. This would allow for modelling and learning from the data the length or size of the extremal cascade (k) and the distribution of the pathway taken by it (say, $4 \rightarrow 1 \rightarrow 2 \rightarrow 3$ or $3 \rightarrow 2 \rightarrow 1 \rightarrow 4$ as two examples of realizations of the chain of extremes).

We leave these open problems to future work.

Acknowledgements We thank members of GAIL (UoE Generative AI Lab), ECFI (Edinburgh Centre for Financial Innovations), as well of GLE²N (The Glasgow–Edinburgh Extremes Network) for insightful discussions and feedback. MdC is partially supported by the Royal Society of Edinburgh and by Abdn via the UoE Centre for Investing Innovation. Finally, funding from Fundação para a Ciência e a Tecnologia under grants <https://doi.org/10.54499/UIDB/04106/2020> and <https://doi.org/10.54499/UIDP/04106/2020> is gratefully acknowledged.

Conflicts of interest The authors declare that they have no conflict of interest.

Data availability statement The datasets are available from the authors and will be included in the R package DATAstudio upon the acceptance of this paper (<https://cran.r-project.org/web/packages/DATAstudio/>).

Software Codes are publicly available from Github (<https://edin.ac/4gJxP2U>).

References

- Alcacer, A., Martinez-Garcia, M., and Epifanio, I. (2024). Ordinal classification for interval-valued data and interval-valued functional data. *Expert Systems with Applications*, 238:122277.
- Allouche, M., Girard, S., and Gobet, E. (2022). EV-GAN: Simulation of extreme events with ReLU neural networks. *Journal of Machine Learning Research*, 23(150):1–39.
- Beirlant, J., Goegebeur, Y., Segers, J., and Teugels, J. (2004). *Statistics of Extremes: Theory and Applications*. Wiley, Hoboken, NJ.
- Berlyand, L. and Jabin, P.-E. (2023). *Mathematics of Deep Learning: An Introduction*. de Gruyter, Boston.
- Bhatia, S., Jain, A., and Hooi, B. (2021). Exgan: Adversarial generation of extreme samples. In *Proceedings of the AAAI Conference on Artificial Intelligence*, volume 35, pages 6750–6758.
- Bishop, C. M. and Bishop, H. (2023). *Deep Learning: Foundations and Concepts*. Springer, New York.
- Coles, S. (2001). *An Introduction to Statistical Modeling of Extreme Values*. Springer, London.
- Cutter, S. L. (2018). Compound, cascading, or complex disasters: What’s in a name? *Environment: Science and Policy for Sustainable Development*, 60(6):16–25.
- de Haan, L. and Ferreira, A. (2006). *Extreme Value Theory: An Introduction*. Springer, New York.
- Dunn, P. K. and Smyth, G. K. (1996). Randomized quantile residuals. *Journal of Computational and Graphical Statistics*, 5:236–244.
- Embrechts, P., Hofert, M., and Wang, R. (2016). Bernoulli and tail-dependence compatibility. *The Annals of Applied Probability*, 26(3):1636–1658.
- Fakhoury, D., Fakhoury, E., and Speleers, H. (2022). Exspline: An interpretable and expressive spline-based neural network. *Neural Networks*, 152:332–346.
- Frank, E. and Hall, M. (2001). A simple approach to ordinal classification. In *Proceedings of the European Conference on Machine Learning (ECML)*, volume 2167 of *Lecture Notes in Computer Science*. Springer, Berlin, Heidelberg.
- Hawkes, A. G. (1971). Point spectra of some mutually exciting point processes. *Journal of the Royal Statistical Society Series B: Statistical Methodology*, 33(3):438–443.
- Horváth, L. and Kokoszka, P. (2012). *Inference for Functional Data with Applications*. Springer, New York.
- Karpov, O. E., Grubov, V. V., Maksimenko, V. A., Kurkin, S. A., Smirnov, N. M., Utyashev, N. P., Andrikov, D. A., Shusharina, N. N., and Hramov, A. E. (2022). Extreme value theory inspires explainable machine learning approach for seizure detection. *Scientific Reports*, 12(1):11474.
- Kokoszka, P. (2017). *Introduction to Functional Data Analysis*. Chapman & Hall/CRC, Boca Raton, FL.
- Laub, P. J., Lee, Y., and Taimre, T. (2021). *The elements of Hawkes processes*. Springer, New York.
- Lee, J., de Carvalho, M., Rua, A., and Avila, J. (2024). Bayesian smoothing for time-varying extremal dependences. *Journal of the Royal Statistical Society, Ser. C*, 73:581–597.
- Lin, J.-N. and Unbehauen, R. (1993). On the realization of a Kolmogorov network. *Neural Computation*, 5(1):18–20.
- Liu, Z., Wang, Y., Vaidya, S., Ruehle, F., Halverson, J., Soljačić, M., Hou, T. Y., and Tegmark, M. (2024). KAN: Kolmogorov–Arnold networks. *arXiv:2404.19756*.
- Montanelli, H. and Yang, H. (2020). Error bounds for deep ReLU networks using the Kolmogorov–Arnold superposition theorem. *Neural Networks*, 129:1–6.
- Murphy, K. P. (2012). *Machine Learning: A Probabilistic Perspective*. MIT press, Cambridge, MA.
- NS, K. S., Wang, Y., Schram, M., Drgona, J., Halappanavar, M., Liu, F., and Li, P. (2024). Extreme risk mitigation in reinforcement learning using extreme value theory. *Transactions on Machine Learning Research*, 05/2024.
- Pytlak, R. (2008). *Conjugate gradient algorithms in nonconvex optimization*, volume 89. Springer, New York.
- Raymond, C., Horton, R. M., Zscheischler, J., Martius, O., AghaKouchak, A., Balch, J., Bowen, S. G., Camargo, S. J., Hess, J., Kornhuber, K., et al. (2020). Understanding and managing connected extreme events. *Nature Climate Change*, 10(7):611–621.
- Resnick, S. I. (2007). *Heavy-Tail Phenomena: Probabilistic and Statistical Modeling*. Springer, New York.
- Rodu, J. and Kafadar, K. (2021). The q-q boxplot. *Journal of Computational and Graphical Statistics*, 31:1–21.
- Sprecher, D. A. and Draghici, S. (2002). Space-filling curves and Kolmogorov superposition-based neural networks. *Neural Networks*, 15(1):57–67.
- Thas, O., Neve, J. D., Clement, L., and Ottoy, J.-P. (2012). Probabilistic index models. *Journal of the Royal Statistical Society Series B: Statistical Methodology*, 74(4):623–671.